Detection of Shortwave-Infrared Cerenkov Luminescence from Medical Isotopes

Benedict E. Mc Larney[1,2], Qize Zhang[1,2], Edwin C. Pratt[1,2], Magdalena Skubal[1,2], Elizabeth Isaac[1,2], Hsiao-Ting Hsu[1,2], Anuja Ogirala[1,2], and Jan Grimm[1–5]

[1]Molecular Pharmacology Program, Memorial Sloan Kettering Cancer Center, New York, New York; [2]Molecular Imaging Therapy Service, Memorial Sloan Kettering Cancer Center, New York, New York; [3]Pharmacology Program, Weill Cornell Medical College, New York, New York; [4]Department of Radiology, Memorial Sloan Kettering Cancer Center, New York, New York; and [5]Department of Radiology, Weill Cornell Medical Center, New York, New York

Medical radioisotopes produce Cerenkov luminescence (CL) from charged subatomic particles ($\beta^{+/-}$) traveling faster than light in dielectric media (e.g., tissue). CL is a blue-weighted and continuous emission, decreasing proportionally to increasing wavelength. CL imaging (CLI) provides an economic PET alternative with the advantage of also being able to image β^- and α emitters. Like any optical modality, CLI is limited by the optical properties of tissue (scattering, absorption, and ambient photon removal). Shortwave-infrared (SWIR, 900–1700 nm) CL has been detected from MeV linear accelerators but not yet from keV medical radioisotopes. **Methods:** Indium-gallium-arsenide sensors and SWIR lenses were mounted onto an ambient light-excluding preclinical enclosure. An exposure and processing pipeline was developed for SWIR CLI and then performed across 6 radioisotopes at in vitro and in vivo conditions. **Results:** SWIR CL was detected from the clinical radioisotopes ^{90}Y, ^{68}Ga, ^{18}F, ^{89}Zr, ^{131}I, and ^{32}P (biomedical research). SWIR CLI's advantage over visible-wavelength (VIS) CLI (400–900 nm) was shown via increased light penetration and decreased scattering at depth. The SWIR CLI radioisotope sensitivity limit (8.51 kBq/μL for ^{68}Ga), emission spectrum, and ex vivo and in vivo examples are reported. **Conclusion:** This work shows that radioisotope SWIR CLI can be performed with unmodified commercially available components. SWIR CLI has significant advantages over VIS CLI, with preserved VIS CLI features such as radioisotope radiance levels and dose response linearity. Further improvements in SWIR optics and technology are required to enable widespread adoption.

Key Words: SWIR; Cerenkov; luminescence; radioisotopes; preclinical

J Nucl Med 2023; 64:177–182
DOI: 10.2967/jnumed.122.264079

Subatomic relativistic particles generate Cerenkov luminescence (CL) in dielectric media (*1*). The traveling particle polarizes surrounding molecules, which generate luminescence upon relaxation (*2*), with CL being ultraviolet-weighted. CL production decreases exponentially with increasing wavelength ($1/\lambda^2$) (*3*). CL's intensity, but not the spectrum profile, correlates with the energy of the emitted particle and has been used in astrophysics, nuclear physics, and recently in biomedical imaging (*4,5*). CL imaging (CLI) is a cost- and time-effective PET alternative for surface-weighted imaging, for example, for triaging patients into those who do not need PET and those who do (*2,6,7*). CLI has focused on CL detection from clinical β- ($\beta^{+/-}$) emitting radioisotopes and linear accelerators (LINAC) (*4,8,9*). Preclinical discoveries and the development of novel targeted radiotracers, dosimetry, and radiotherapy-based treatments have been aided by CLI (*10,11*). Clinical CLI has also found applications in image-guided surgery for detecting margins, determining the clinical uptake of radiotracers, and making real-time dosimetry readings (*7,12–15*).

Single-photon-sensitive devices responsive to the CL spectrum are readily available, including low-dark-noise and low-read-noise optical devices (*2*). However, visible wavelength (VIS) CLI (400–900 nm) suffers significant drawbacks in preclinical and clinical settings. Endogenous chromophores limit the achievable VIS CL penetration depths, with scattering further reducing the resolution, contrast, and sensitivity of VIS CLI at depth (*16,17*). Optical imaging has shifted to longer wavelengths at which light absorption and scattering are reduced (*18*). Near-infrared (NIR) imaging (>650 nm) reduces absorption by approximately 2 orders of magnitude over VIS imaging (*16,19*). Studies have used dyes and nanoparticles for the red-shifted conversion of CL (*20–22*). Shortwave-infrared (SWIR) imaging (900–1,700 nm) has shown that tissue absorption, scattering, and autofluorescence are of negligible levels (*23*). SWIR's advantages for resolution and contrast have been shown via the clinically approved indocyanine green (*24*). Förster resonance energy transfer–based SWIR CL has been achieved via x-ray-excited nanoprobes and LINAC-excited emission of quantum dots (*20,25–27*). LINAC SWIR CLI was demonstrated without secondary emitters, showing improvements over VIS-NIR CLI (*28*). However, radioisotopes produce CL that is an order of magnitude dimmer than LINACs and are therefore more demanding to image (LINAC, 6–24 MeV; ^{68}Ga, 0.836 MeV) (*29–32*). Radioisotope CLI requires complete exclusion of ambient light combined with efficient optical imaging systems and cannot be pulse-synchronized in its acquisition as LINAC CLI can (*30,33*). The already low CL radiance of radioisotopes is further reduced at SWIR wavelengths, magnifying the difficulty of SWIR CL detection (*3*). Nevertheless, in this work SWIR CLI from radioisotopes was achieved via unmodified and commercially available imaging components and revealed defined advantages over VIS CLI.

MATERIALS AND METHODS

Radioisotope SWIR Setup

SWIR CLI was achieved via commercially available indium-gallium-arsenide focal plane arrays (NIRVana 640 TE [Teledyne Princeton] or ZephIR 1.7 [Photon etc. Inc.]) and a SWIR lens set to $f/1.4$ (SWIR-16 [Navitar] or 8-mm SWIR lens 83-815 [Edmund Optics]) mounted on an

Received Feb. 28, 2022; revision accepted Jun. 11, 2022.
For correspondence or reprints, contact Jan Grimm (grimmj@mskcc.org).
Published online Jun. 23, 2022.
COPYRIGHT © 2023 by the Society of Nuclear Medicine and Molecular Imaging.

enclosure (Fig. 1). Figures 1B–1E were acquired without optical filters (NIRVana 640 TE, 900–1,700 nm) (*34*). All other figures used a 650- or 900-nm optical density 4.0 long-pass filter (Edmund Optics 84-759 and 84-764). Acquisition (ninety 10s frames [15 min]) was controlled via respective acquisition software. Equivalent dark noise was recorded and subtracted for each sensor. White-light images were acquired with room lights on and enclosure door open as the room lights had SWIR spectral emission (Pentron 3000K; Osram Sylvania) (*35*). Radioisotopes were imaged in suitable containers within a lead pig. Black posterboard (TB5; Thorlabs) was used to block CL and allow γ particles to pass.

Determining the Radioisotope SWIR CLI Temporal Resolution and Emission Spectrum

The SWIR CL temporal resolution and emission spectrum were determined using 370 MBq of ^{32}P in 1 mL of water (β^- average, 0.695 MeV; half-time, 14.3 d; NEX060005MC [Perkin Elmer]). Ninety-frame acquisitions at respective exposure times were performed (Fig. 1D; Supplemental Fig. 1; supplemental materials are available at http://jnm.snmjournals.org). The limit of detection was defined as when SWIR CL was not determinable from the noise. Long-pass filters (1,000–1,500 nm in 100-nm steps (FELH1000:100:

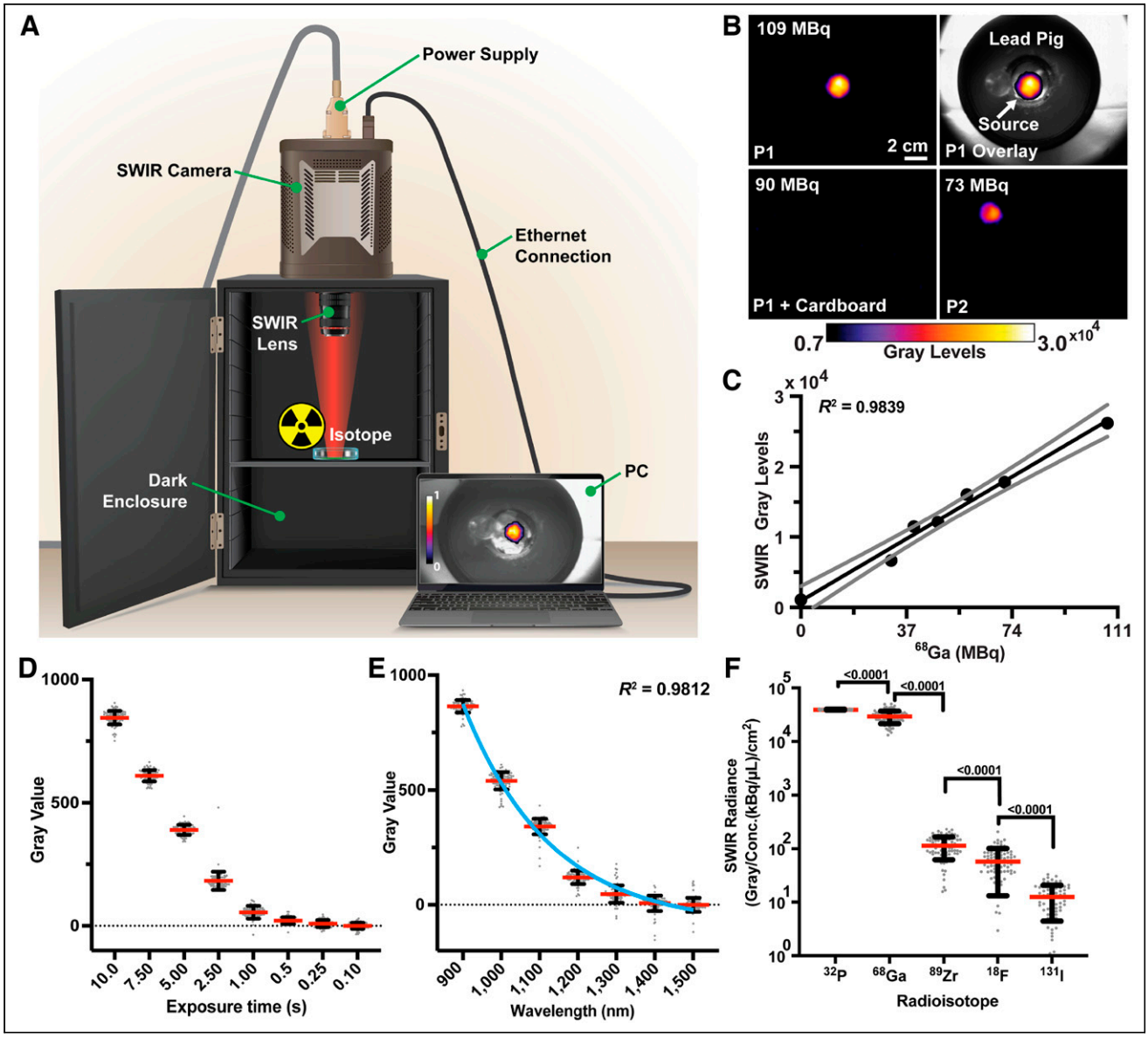

FIGURE 1. SWIR CL radioisotope imaging setup and characterization. (A) A dark enclosure was used for all imaging. Mounted on the camera was a 16 or 8 mm f/1.4 SWIR lens. (©2022 Memorial Sloan Kettering Cancer Center. All rights reserved.) (B) Linearity assessment of the camera via ^{68}Ga imaged at positions (P1, P2) across the field of view, with P1 + cardboard confirming that detection was not as a result of γ strikes. (C) SWIR gray levels and corresponding ^{68}Ga activity (MBq). Linear regression and 95% CIs are shown (Pearson $R^2 = 0.9839$, 2-tailed $P < 0.0001$). SWIR CLI is linearly responsive and quantitative as found with VIS CLI. (D) ^{32}P SWIR gray-value intensity in relation to exposure time changes. (E) Graphical representation of radioisotope (^{32}P) SWIR CL emission spectrum from 900 to 1,500 nm, with the blue line representing a 1-phase exponential decay function ($R^2 = 0.9812$). Inherent system noise, low photon production, and water absorption prevent detection > 1,400 nm. (F) Descending radioisotope radiance (^{32}P, ^{68}Ga, ^{89}Zr, ^{18}F, and ^{131}I) corrected for concentration (kBq/μL) and spatial field of view (cm^2). Student t test (unpaired, 2-sided) P values are shown. In all cases, mean measurements (red line), SDs (black lines), and individual measurements ($n = 90$ technical replicates, gray dots) are shown, for radiance comparison negative values were excluded.

1500, SM1L03, and SM1A57; Thorlabs) elucidated the SWIR radioisotope spectrum.

Image Processing and Statistical Analysis

Fiji (ImageJ, version 2.0 (*36*)) was used for image processing (Supplemental Fig. 2). Dark noise was subtracted from the data followed by binning (8 × 8, to improve sensitivity), median filtering (outlier, γ strike removal), fast-Fourier-transform bandpass transformations (artifact removal), and rolling-ball background subtraction (*37*). Images were resized for white-light overlays. Statistical analysis graphing was performed in Prism, version 9 (GraphPad Software LLC). Statistical analyses and replicate information are shown in all cases. Radiance was calculated via gray values corrected for isotope concentration (kBq/μL) and field of view (cm^2). Full width at half maximum was measured in MATLAB (version 2020b; MathWorks Inc.).

Silica Nanoparticle Radiolabeling and Injection

Silica nanoparticles (SiNPs) were labeled with ^{68}Ga or ^{90}Y as previously described (*38*). SiNPs were incubated with free isotope at a pH of 8.8 for 60 min, on a thermomixer at 70°C and 500 rpm. Radiolabeled SiNPs were resuspended in 30 μL of saline for footpad injection.

Preclinical SWIR CLI

All experiments were performed in accordance with Institutional Animal Care and Use Committee guidelines at Memorial Sloan Kettering Cancer Center and with National Institutes of Health guidance on the care and use of laboratory animals. Three percent isoflurane in 100% O_2 v/v was followed by 1%–2% isoflurane in 100% O_2 v/v for maintenance of anesthesia; euthanasia was performed using CO_2 in accordance with approved protocols. All mice (10 in total, FoxN1^{NU}, stock no. 069; Envigo) were suitably housed with food and water ad libitum. Four xenograft mice were generated by injecting 0.3 × 10^6 4T1 cells (ATCC, CRL-2539) suspended in 30 μL of Matrigel (catalog no. 354234; Corning) into the fourth mammary fat pad (Supplemental Fig. 3). Three euthanized xenografted mice were injected (mice were randomized to receive a range of activity from 0–166.5 MBq) with up to 166.5 MBq of ^{18}F-FDG, with 1 mouse acting as a negative control. One non-xenografted euthanized mouse was injected into the footpad with ^{68}Ga-labeled SiNPs. Four non-xenografted mice were injected with ^{90}Y-labeled SiNPs, with an additional mouse acting as a negative control for in vivo experiments.

RESULTS

Confirmation of SWIR CL Detection from Radioisotopes

In Figure 1A, the SWIR CLI radioisotope setup is shown detecting ^{68}Ga suspended in 0.1 M HCl (*39,40*). Figure 1B shows the processed SWIR CL image overlaid onto the white-light image. This demonstrates that SWIR signal is coming from ^{68}Ga and that the processing steps sufficiently removed γ strikes while retaining CL signals. CL detection is further confirmed by a lack of signal when cardboard was placed over the sample, blocking light but not the highly energetic photons from ^{68}Ga's decay (e.g., 511 and 1,077 keV). The ^{68}Ga source was further moved and detected around the field of view, decaying in the process, visible via a decreasing SWIR signal, following the decay half-life of the isotope. Manual regions of interest were measured to determine the signal intensity (gray values) of the sensor for each position and time point. SWIR CLI showed quantitative linearity to ^{68}Ga levels, as previously reported for VIS CLI (*4*). We then successfully detected 4 additional radioisotopes under comparative conditions: ^{32}P,^{18}F, ^{89}Zr, and ^{131}I (Fig. 1; Supplemental Fig. 4). The SWIR radiance of each was calculated as before (Fig. 1), with values corrected for concentration (kBq/μL) and spatial field of view (cm^2). SWIR CLI readily differentiated the tested radioisotopes in line with VIS CLI, as shown by the *P* values in Figure 2B (*41,42*). Theoretically ^{68}Ga has a higher radiance than ^{32}P; however, the increased sensor strikes from 511- and 1,077-keV photons by ^{68}Ga prevent SWIR CLI from confirming this, as the setup did not incorporate lead shielding (*42*).

SWIR CLI Radioisotope Temporal Detection Limit and Emission Spectrum

The system was characterized using ^{32}P (β^-), with concentrations used to facilitate SWIR CLI at a temporal resolution of 0.25 s (Fig, 1; Supplemental Fig, 1). ^{32}P's radiance and half-life enabled determination of the radioisotope SWIR CL emission spectrum (*42*). No filter was used (>920 nm, spectral response of the sensor), and long-pass filtered acquisitions (1,000–1,500 nm, 100-nm steps) were performed. This sensor has a nonthinned indium phosphide substrate bandgap (1.35 eV) preventing detection of light less than 920 nm, and the bandgap of indium-gallium-arsenide (0.75 eV) results in a short-pass cutoff at 1,700 nm (*43–45*). The radioisotope SWIR CL spectrum is shown in Figure 1E, with intensity exponentially decreasing (1-phase

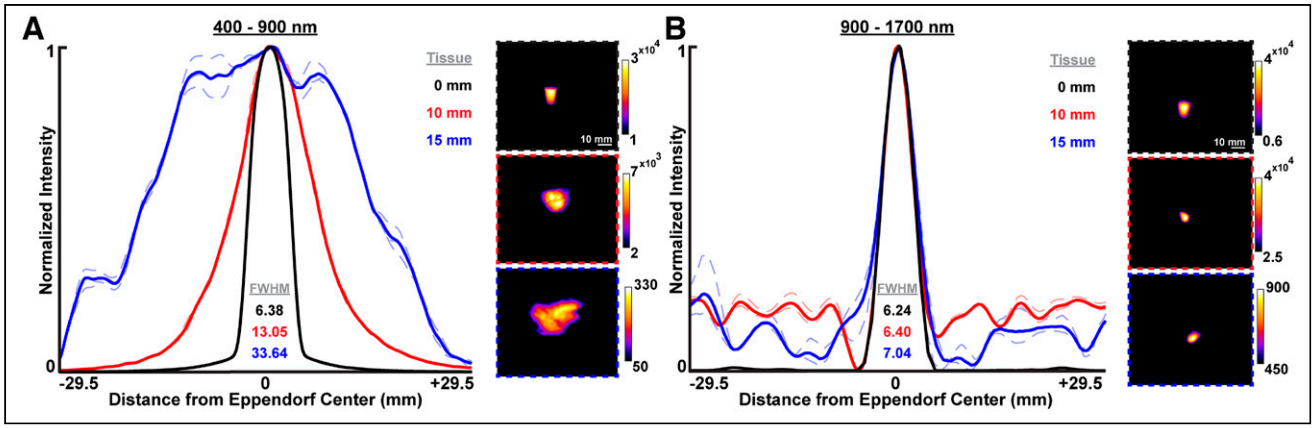

FIGURE 2. Reduced scattering via SWIR CLI (900–1,700 nm) over VIS CLI (400–900 nm). (A) Left, normalized VIS CLI line intensity profiles of a ^{90}Y source (Eppendorf, 55.5 MBq in 200 mL of saline) at increasing scattering tissue depths (chicken breast: 0, 10, and 15 mm). Full widths at half maximum increase with scattering tissue depth at 0, 10, and 15 mm with respective full widths at half maximum of 6.38, 13.05, and 33.64 mm. Right, representative VIS CLI images. (B) Left, normalized SWIR CLI line intensity profiles from the phantom setup with full widths at half maximums of 6.24, 6.40, and 7.04 mm. Right, representative SWIR CL images. In all cases, 3 separate line measurements are made from images at each depth (dotted lines), with mean shown (solid line). FWHM = full width at half maximum.

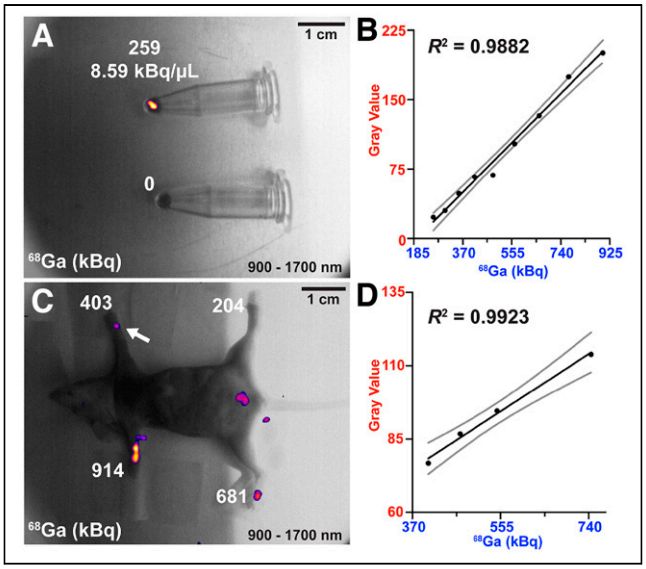

FIGURE 3. In vitro and ex vivo SWIR CLI (900–1,700 nm) radioisotope sensitivity limit for ^{68}Ga radiolabeled SiNPs. (A) SWIR CLI radioisotope in vitro detection limit for ^{68}Ga-SiNPs after multiple half-lives. (B) SWIR CLI decay tracking to the limit of detection, linear regression (solid black line, R^2 = 0.9882) and 95% CIs (solid gray lines) are shown. (C) Ex vivo SWIR CLI limit of detection for ^{68}Ga-labeled SiNPs. The detection limit slightly worsens in tissue compared with in vitro imaging (~140 kBq less sensitive). (D) Linear regression analysis (R^2 = 0.9923) of ex vivo SWIR CLI of ^{68}Ga-labeled SiNPs to limit of detection (403.3 kBq, C), 95% CIs are shown (solid gray lines). Detection limit paw is labeled with a white arrow.

exponential decay, R^2 = 0.9812), as expected and reported for VIS CLI and LINAC SWIR CLI (*2,28*). Detection above 1,400 nm is challenging because of system noise, lens inefficiency, and water absorption (Figs. 1E and 1F; Supplemental Figs. 1 and 7) (*19,46*).

Reduced Scattering via SWIR CLI over VIS CLI

A 55.5-MBq quantity of ^{90}Y in an Eppendorf tube (β^- emitter; average, 0.94 MeV; half-time, 64 h in 200 μL of saline) was imaged on both the SWIR (900–1,700 nm) and the IVIS (PerkinElmer) (VIS CLI, 400–900 nm) imaging systems to assess the advantages of SWIR CLI. ^{90}Y is clinically administered from 0.500 to 5.291 GBq to treat primary liver cancer (hepatocellular carcinoma) and metastases in the liver (*47,48*). Scattering medium (raw chicken breast: 0, 10, and 15 mm) was placed over the source before CLI was performed. Respective exposure times without scattering medium (VIS CLI, 10 s; SWIR CLI, 900 s) were maintained at all tissue depths. SWIR CLI shows an improvement in resolution compared with VIS CLI when imaging through scattering tissue (Fig. 2). In SWIR CLI, the Eppendorf tube shape is consistent up to 15 mm of tissue, whereas the shape is distorted and enlarged over 5 times from scatter in VIS CLI. In this investigation SWIR CLI provided greater resolution at depth than VIS CLI for radioisotope location. This increased accuracy is demonstrated by the full widths at half maximum (6.38, 13.05, and 33.64 mm for VIS CLI and 6.24, 6.40, and 7.04 mm for SWIR CLI at 0, 10, and 15 mm of tissue, respectively) (Fig. 2).

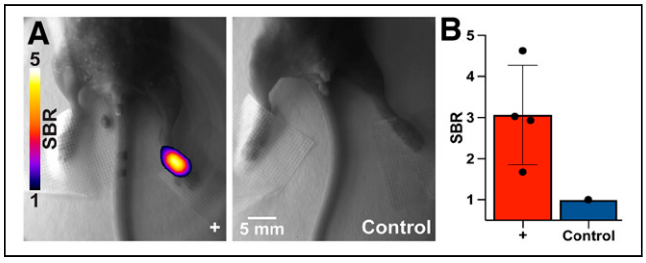

FIGURE 4. In vivo SWIR CLI detection of ^{90}Y-labeled SiNPs 3 h after injection into footpad. (A, left) Representative image of mouse injected (+) with ^{90}Y-labeled SiNPs (~7.4 MBq). (A, right) Image of control mouse without any injection. (B) Quantified signal-to-background ratios of injected (n = 4) vs. control mice (n = 1). All images are shown in respective signal-to-background ratios. SBR = signal-to-background ratio.

Sensitivity Limits of SWIR CLI Radioisotope In Vitro and Ex Vivo

Commercial SWIR sensors are insensitive to light of less than 920 nm without indium phosphide cap thinning. In systems with indium phosphide thinning, the sensor has a largely increased range but is rather insensitive compared with silicon-based electron-multiplying charge-coupled devices. One such SWIR sensor, the ZephIR 1.7x [Photon etc. Inc.]), was used with significantly reduced quantum efficiency in the VIS range (~25% at 600 nm). The sensor enabled a comparison of the spatial localization of radioisotope VIS-SWIR (400–1,700 nm), NIR-SWIR (650–1,700 nm), and SWIR (900–1,700 nm) CLI. ^{68}Ga-conjugated SiNPs (in 30 μL of saline) opposite a nonradiolabeled SiNP control were imaged at VIS-SWIR, NIR-SWIR, and SWIR spectra for numerous half-lives via appropriate long-pass filters. The detected CL signals are localized to the radiolabeled SiNPs throughout the spectra (Supplemental Figs. 5A–5D). The phantom detection limit of radioisotope SWIR CLI was 259 kBq (8.51 kBq/μL) for ^{68}Ga-labeled SiNPs (Figs. 3A–3B). Theoretical limits for radioisotopes tested here in SWIR CLI are shown in Supplemental Table 1 (*42*).

Next, the SWIR CLI detection limit in tissue was assessed. A euthanized mouse received 30 μL of respective paw injections of varying ^{68}Ga-SiNP activities. As can be seen in Figures 3C–3D, ^{68}Ga-SiNPs were detected via SWIR CLI down to 403.3 kBq, within clinically administered levels (~148 MBq) (*49*).

In Vivo Detection of Radioisotope SWIR CLI

^{90}Y conjugated to SiNPs was used for in vivo SWIR CLI radioisotope detection (*38*). ^{90}Y has been shown to improve the SNR of CL detection over, for example, ^{18}F or ^{68}Ga because of reduced γ sensor strikes (*50*). During in vivo imaging, the long exposure times for SWIR CLI contaminated the SWIR CL image with thermal signatures (removed in postprocessing via rolling-ball background subtraction), complicating SWIR CLI over VIS CLI. Mice were injected with approximately 7.4 MBq of ^{90}Y-labeled SiNPs into a single footpad and imaged 3 h later. ^{90}Y is administered clinically for radioembolization at activities ranging from 500 to 5,291 MBq (*47,48*). The resulting SWIR CLI signal was readily detected over background thermal signatures present in vivo (4 mice; Fig. 4; Supplemental Fig. 6). Footpad-injected radiolabeled SiNPs slowly migrate through the lymphatic system (48 h), preventing CL contamination of the endogenous thermal signature (*38*). Respective residual thermal signatures remaining after background subtraction from each mouse were used to divide the image, producing measurements in terms of signal-to-thermal-background ratio (Supplemental Fig. 2). Signal-to-background ratios from injected mice ranged from 1.68 to 4.63, with a mean of 3.07 (Fig. 4B).

DISCUSSION

This work aimed to detect the theoretical SWIR CL emission from clinical radioisotopes via commercially available components (Supplemental Fig. 7). To date, SWIR CL has been detected only

from LINAC sources, which produce CL that is an order of magnitude brighter (*25,28*). The devised setup and enclosure provided ambient light-free imaging (*51,52*). The state-of-the-art thermoelectric cooled (TEC) SWIR sensors used in our study produce dark noise 2–3 orders of magnitude higher than cameras based on silicon electron-multiplying charge-coupled devices. This intrinsic noise within the SWIR setup, an obstacle not only for SWIR CLI, has been the main limiting factor throughout this work (*53*). In addition, the even further reduced light output at longer wavelengths necessitated longer exposure times (minutes for SWIR CLI vs. seconds for VIS CLI). Nevertheless, the radioisotopes we explored produced detectable SWIR CL (Fig. 1), with relative radiances in line with VIS CLI (*3,41,42*). Importantly, SWIR CLI increased linearly with radioisotope levels (Fig. 1; Fig. 3). SWIR CLI radioisotope sensitivity was found to be 259 kBq (8.51 kBq/μL) in vitro and 403.3 kBq in tissue with ^{68}Ga. VIS CLI is 4 orders of magnitude more sensitive, with ^{68}Ga detection reported at 0.00333 kBq/μL (*54*). The insensitivity of SWIR CLI limits applications with the current generation of SWIR cameras. However, its advantage of reduced scattering in combination with the increased transmission of CL in the SWIR region (Fig. 2; Supplemental Fig. 7), potentially paired with SWIR-void room lighting, could open new applications for radioisotope SWIR CLI (*28*) without light-excluding enclosures that also benefit from improved radioisotope resolution at depth. Combining the strengths of indium-gallium-arsenide–based (900–1,700 nm) and silicon-based (400–900 nm) sensors would open further applications for CLI and is worth investigating (*16,19,46,55,56*). Assuming sufficient radioisotope levels, SWIR CLI can be performed close to video rates (0.25 s; Fig. 1).

The detected radioisotope SWIR CL spectrum was found to be in line with the SWIR LINAC spectrum (*28*). Similarly to SWIR LINAC CL, theoretically emitted CL above 1,400 nm could not be reliably detected, likely because of sensor noise and water absorption (Supplemental Fig. 7). However, the advantage of wavelengths above 1,400 nm compared with 900–1,300 nm is unclear for SWIR CLI in any case because of the increased absorption of water above 1,300 nm (*19,46*).

The preclinical applicability of SWIR CL was investigated and initially focused on the ex vivo SWIR CLI of intratumorally injected ^{18}F-FDG (Supplemental Fig. 3). The weak CL of ^{18}F (26 times dimmer than ^{68}Ga) required 1h acquisition times for accurate signal detection (*42,54*). ^{90}Y was used to overcome the limitations of ^{68}Ga and ^{18}F for this investigation (negligible γ emission, brighter CL, longer half-life than ^{68}Ga, 64.2 h vs. 1.13 h) (*2,41*). ^{90}Y-labeled SiNPs were injected into the footpad of live mice for in vivo SWIR CLI detection (*38*). Mice were imaged 3 h after injection (~7.4 MBq of ^{90}Y-SiNPs) together with a noninjected control mouse. Exposure times of 15 min along with suitable image processing steps provided a reliable SWIR CL signal that was detected over the endogenous thermal signature and inherent noise (Fig. 4).

CONCLUSION

Our study presents the first example and proof-of-principle of in vivo radioisotope SWIR CLI. Considering the optical properties of tissue, it has been shown that most CL emitted from tissue at depth is above 600 nm (*3,16*). Therefore, the ideal radioisotope CL camera would be one that combines the spectral range of thinned SWIR sensors (600–1,700 nm, see Supplemental Fig. 7) with the photon sensitivity of sensors based on silicon electron-multiplying charge-coupled devices. Future iterations of SWIR CLI should aim to tackle its main limitations via improved lenses (f/0.95) and a dark-noise–reduced camera sensor to improve overall sensitivity, along with lead shielding to further increase sensitivity via γ strike reduction. Such components would be highly customized and outside the scope of this proof-of-principle work. Human eyes respond to light from approximately 400 to 700 nm, and by changing ambient lighting to non–SWIR-emitting light-emitting diodes, radioisotope SWIR CLI might be performed in a well-lit room and without the need for a dark enclosure, as achieved for VIS and SWIR LINAC CLI (*7,30*). This would directly impact radioisotope preclinical CLI, which is a common, fast, and cost-effective PET alternative for novel radiotracers and treatment tracking (*57,58*). However, significant improvements are required in SWIR optics and technology before this can be realized.

DISCLOSURE

Funding was in part provided by National Institutes of Health NCI grants R01CA183953 (to Jan Grimm) and P30 CA08748 (to Craig Thompson/Memorial Sloan Kettering Cancer Center). No other potential conflict of interest relevant to this article was reported.

ACKNOWLEDGMENTS

We thank Craig Wall, Manjul Shah, Sabbir Liakat, and Princeton Teledyne for providing the NIRvana 640 TE camera and lens; Photon etc. for the Zephir 1.7x camera; and Valerie Longo and Pat Zanzonico of Memorial Sloan Kettering Cancer Center for animal experiment assistance and logistics of equipment setup.

KEY POINTS

QUESTION: SWIR CLI (900–1,700 nm) has so far only been detected from LINACs. Is it possible to detect SWIR CLI from radioisotopes, orders of magnitude dimmer?

PERTINENT FINDINGS: This work detected SWIR CLI via commercially available components from numerous preclinical and clinical radioisotopes, with the radiances and spectrum performing in a manner consistent with VIS CLI (400–900 nm).

IMPLICATIONS FOR PATIENT CARE: SWIR CLI has distinct advantages over VIS CLI in terms of reduced scattering and absorption at depth; however, significant technologic and optical improvements are required for comparable sensitivity.

REFERENCES

1. Cherenkov PA. Visible light from clear liquids under the action of gamma radiation. *C.R. (Dokl.) Acad. Sci. URSS* 1934;2:451–454. [Phyaico-Mathematicat Institute V.A. Stekiova. Academy of Science. Leningrad. USSR].
2. Ciarrocchi E, Belcari N. Cerenkov luminescence imaging: physics principles and potential applications in biomedical sciences. *EJNMMI Phys.* 2017;4:14.
3. Glaser AK, Zhang R, Andreozzi JM, Gladstone DJ, Pogue BW. Cherenkov radiation fluence estimates in tissue for molecular imaging and therapy applications. *Phys Med Biol.* 2015;60:6701–6718.
4. Ruggiero A, Holland JP, Lewis JS, Grimm J. Cerenkov luminescence imaging of medical isotopes. *J Nucl Med.* 2010;51:1123–1130.
5. Contalbrigo M, Kubarovsky V, Mirazita M, et al. The CLAS12 ring imaging Cherenkov detector. *Nucl Instrum Methods Phys Res A.* 2020;964:163791.
6. Mitchell GS, Gill RK, Boucher DL, Li C, Cherry SR. In vivo Cerenkov luminescence imaging: a new tool for molecular imaging. *Philos Trans A Math Phys Eng Sci.* 2011;369:4605–4619.
7. Pratt EC, Skubal M, Mc Larney B, et al. Prospective testing of clinical Cerenkov luminescence imaging against standard-of-care nuclear imaging for tumour location. *Nat Biomed Eng.* 2022;6:559–568.

8. Tamura R, Pratt EC, Grimm J. Innovations in nuclear imaging instrumentation: Cerenkov imaging. Semin Nucl Med. 2018;48:359–366.
9. Miao T, Bruza P, Pogue BW, et al. Cherenkov imaging for Linac beam shape analysis as a remote electronic quality assessment verification tool. *Med Phys.* 2019;46:811–821.
10. D'Souza JW, Hensley H, Doss M, et al. Cerenkov luminescence imaging as a modality to evaluate antibody-based PET radiotracers. *J Nucl Med.* 2017;58:175–180.
11. Lohrmann C, Zhang H, Thorek DL, et al. Cerenkov luminescence imaging for radiation dose calculation of a ^{90}Y-labeled gastrin-releasing peptide receptor antagonist. *J Nucl Med.* 2015;56:805–811.
12. Olde Heuvel J, de Wit-van der Veen BJ, van der Poel HG, et al. ^{68}Ga-PSMA Cerenkov luminescence imaging in primary prostate cancer: first-in-man series. *Eur J Nucl Med Mol Imaging.* 2020;47:2624–2632.
13. Thorek DL, Riedl CC, Grimm J. Clinical Cerenkov luminescence imaging of ^{18}F-FDG. *J Nucl Med.* 2014;55:95–98.
14. Grootendorst MR, Cariati M, Pinder SE, et al. Intraoperative assessment of tumor resection margins in breast-conserving surgery using ^{18}F-FDG Cerenkov luminescence imaging: a first-in-human feasibility study. *J Nucl Med.* 2017;58:891–898.
15. Jarvis LA, Zhang R, Gladstone DJ, et al. Cherenkov video imaging allows for the first visualization of radiation therapy in real time. *Int J Radiat Oncol Biol Phys.* 2014;89:615–622.
16. Jacques SL. Optical properties of biological tissues: a review. *Phys Med Biol.* 2013;58:R37–R61.
17. Yaroshevsky A, Glasser Z, Granot E, Sternklar S. Transition from the ballistic to the diffusive regime in a turbid medium. *Opt Lett.* 2011;36:1395–1397.
18. Ding F, Zhan Y, Lu X, Sun Y. Recent advances in near-infrared II fluorophores for multifunctional biomedical imaging. *Chem Sci.* 2018;9:4370–4380.
19. Cao Q, Zhegalova NG, Wang ST, Akers WJ, Berezin MY. Multispectral imaging in the extended near-infrared window based on endogenous chromophores. *J Biomed Opt.* 2013;18:101318.
20. Thorek DL, Ogirala A, Beattie BJ, Grimm J. Quantitative imaging of disease signatures through radioactive decay signal conversion. *Nat Med.* 2013;19:1345–1350.
21. Zhang Q, Pratt EC, Tamura R, et al. Ultrasmall downconverting nanoparticle for enhanced Cerenkov imaging. *Nano Lett.* 2021;21:4217–4224.
22. Pratt EC, Shaffer TM, Zhang Q, Drain CM, Grimm J. Nanoparticles as multimodal photon transducers of ionizing radiation. *Nat Nanotechnol.* 2018;13:418–426.
23. Thimsen E, Sadtler B, Berezin MY. Shortwave-infrared (SWIR) emitters for biological imaging: a review of challenges and opportunities. *Nanophotonics.* 2017;6:1043–1054.
24. Carr JA, Franke D, Caram JR, et al. Shortwave infrared fluorescence imaging with the clinically approved near-infrared dye indocyanine green. *Proc Natl Acad Sci USA.* 2018;115:4465–4470.
25. Naczynski DJ, Sun C, Türkcan S, et al. X-ray-induced shortwave infrared biomedical imaging using rare-earth nanoprobes. *Nano Lett.* 2015;15:96–102.
26. Cao X, Jiang S, Jia MJ, et al. Cherenkov excited short-wavelength infrared fluorescence imaging in vivo with external beam radiation. *J Biomed Opt.* 2018;24:1–4.
27. Dothager RS, Goiffon RJ, Jackson E, Harpstrite S, Piwnica-Worms D. Cerenkov radiation energy transfer (CRET) imaging: a novel method for optical imaging of PET isotopes in biological systems. *PLoS One.* 2010;5:e13300.
28. Cao X, Jiang S, Jia M, et al. Observation of short wavelength infrared (SWIR) Cherenkov emission. *Opt Lett.* 2018;43:3854–3857.
29. Glaser AK, Zhang R, Gladstone DJ, Pogue BW. Optical dosimetry of radiotherapy beams using Cherenkov radiation: the relationship between light emission and dose. *Phys Med Biol.* 2014;59:3789–3811.
30. Glaser AK, Zhang R, Davis SC, Gladstone DJ, Pogue BW. Time-gated Cherenkov emission spectroscopy from linear accelerator irradiation of tissue phantoms. *Opt Lett.* 2012;37:1193–1195.
31. Browne E. Commonly used radioactive sources. *Eur Phys J C.* 2000;15:190.
32. Pritychenko B, Běták E, Kellett M, Singh B, Totans J. The nuclear science references (NSR) database and web retrieval system. *Nucl Instrum Methods Phys Res A.* 2011;640:213–218.
33. Tendler II, Hartford A, Jermyn M, et al. Experimentally observed Cherenkov light generation in the eye during radiation therapy. *Int J Radiat Oncol Biol Phys.* 2020;106:422–429.
34. Huang Y-H, Yang C-C, Peng T-C, et al. 10-Gb/s InGaAs p-i-n photodiodes with wide spectral range and enhanced visible spectral response. *IEEE Photonics Technol Lett.* 2007;19:339–341
35. Elvidge CD, Keith DM, Tuttle BT, Baugh KE. Spectral identification of lighting type and character. *Sensors (Basel).* 2010;10:3961–3988.
36. Schindelin J, Arganda-Carreras I, Frise E, et al. Fiji: an open-source platform for biological-image analysis. *Nat Methods.* 2012;9:676–682.
37. Walter J. FFT filter. ImageJ website. https://imagej.nih.gov/ij/plugins/fft-filter.html. Published October 29, 2001. Updated March 26, 2007. Accessed June 30, 2022.
38. Shaffer TM, Wall MA, Harmsen S, et al. Silica nanoparticles as substrates for chelator-free labeling of oxophilic radioisotopes. *Nano Lett.* 2015;15:864–868.
39. Darr C, Harke NN, Radtke JP, et al. Intraoperative ^{68}Ga-PSMA Cerenkov luminescence imaging for surgical margins in radical prostatectomy: a feasibility study. *J Nucl Med.* 2020;61:1500–1506.
40. Banerjee SR, Pomper MG. Clinical applications of gallium-68. *Appl Radiat Isot.* 2013;76:2–13.
41. Beattie BJ, Thorek DL, Schmidtlein CR, Pentlow KS, Humm JL, Hielscher AH. Quantitative modeling of Cerenkov light production efficiency from medical radionuclides. *PLoS One.* 2012;7:e31402.
42. Gill RK, Mitchell GS, Cherry SR. Computed Cerenkov luminescence yields for radionuclides used in biology and medicine. *Phys Med Biol.* 2015;60:4263–4280.
43. Martin T, Dixon P. InGaAs sees infrared and visible light. *Laser Focus World.* 2004;40:109–111.
44. Williamson JB, Carey KW, Kellert F, Braum D, Hodge L, Loncasty D. High-density, planar Zn-diffused InGaAs/InP photodetector arrays with extended short-wavelength response. *IEEE Trans Electron Dev.* 1991;38:2707.
45. Hoelter TR, Barton JB. Extended short-wavelength spectral response from InGaAs focal plane arrays. Spie Digital Library website. https://doi.org/10.1117/12.515397. October 10, 2003. Accessed September 13, 2022.
46. Carr JA, Aellen M, Franke D, So PT, Bruns OT, Bawendi MG. Absorption by water increases fluorescence image contrast of biological tissue in the shortwave infrared. *Proc Natl Acad Sci USA.* 2018;115:9080–9085.
47. Kim SP, Cohalan C, Kopek N, Enger SA. A guide to ^{90}Y radioembolization and its dosimetry. *Phys Med.* 2019;68:132–145.
48. Fidelman N, Kerlan RK Jr, Hawkins RA, et al. Radioembolization with ^{90}Y glass microspheres for the treatment of unresectable metastatic liver disease from chemotherapy-refractory gastrointestinal cancers: final report of a prospective pilot study. *J Gastrointest Oncol.* 2016;7:860–874.
49. Demirci E, Toklu T, Yeyin N, et al. Estimation of the organ absorbed doses and effective dose from ^{68}Ga-PSMA-11 PET scan. *Radiat Prot Dosimetry.* 2018;182:518–524.
50. Carpenter CM, Ma X, Liu H, et al. Cerenkov luminescence endoscopy: improved molecular sensitivity with β^--emitting radiotracers. *J Nucl Med.* 2014;55:1905–1909.
51. Alsheikh H. [P091] Investigation of Cherenkov imaging using IVIS bioluminescence scanner. *Physica Medica.* 2018;52:127.
52. Spinelli AE, Kuo C, Rice BW, et al. Multispectral Cerenkov luminescence tomography for small animal optical imaging. *Opt Express.* 2011;19:12605–12618.
53. Fraenkel R, Berkowicz E, Bikov L, et al. Development of low-SWaP and low-noise InGaAs detectors. Spie Digital Library website. https://doi.org/10.1117/12.2262112. May 3, 2017. Accessed September 13, 2022.
54. olde Heuvel J, de Wit-van der Veen B, Vyas K, et al. Performance evaluation of Cerenkov luminescence imaging: a comparison of ^{68}Ga with ^{18}F. *EJNMMI Phys.* 2019;6:17.
55. Zhang H, Salo DC, Kim DM, Komarov S, Tai Y-C, Berezin MY. Penetration depth of photons in biological tissues from hyperspectral imaging in shortwave infrared in transmission and reflection geometries. *J Biomed Opt.* 2016;21:126006.
56. Golovynskyi S, Golovynska I, Stepanova LI, et al. Optical windows for head tissues in near-infrared and short-wave infrared regions: approaching transcranial light applications. *J Biophotonics.* 2018;11:e201800141.
57. Xu Y, Chang E, Liu H, Jiang H, Gambhir SS, Cheng Z. Proof-of-concept study of monitoring cancer drug therapy with Cerenkov luminescence imaging. *J Nucl Med.* 2012;53:312–317.
58. Liu M, Zheng S, Zhang X, et al. Cerenkov luminescence imaging on evaluation of early response to chemotherapy of drug-resistant gastric cancer. *Nanomedicine.* 2018;14:205–213.